CHEMISTRY OF MATERIALS
Cite This: Chem. Mater. 2017, 29, 10551−10560
Article
pubs.acs.org/cm

Formation of Colloidal Copper Indium Sulfide Nanosheets by Two-Dimensional Self-Organization

Anne C. Berends,[†] Johannes D. Meeldijk,[‡] Marijn A. van Huis,[§] and Celso de Mello Donega*[,†]

[†]Condensed Matter and Interfaces, Debye Institute for Nanomaterials Science, Utrecht University, Princetonplein 5, 3584 CC Utrecht, The Netherlands

[‡]Electron Microscopy Utrecht, Utrecht University, 3584 CH Utrecht, The Netherlands

[§]Soft Condensed Matter, Debye Institute for Nanomaterials Science, Utrecht University, Princetonplein 5, 3584 CC Utrecht, The Netherlands

Supporting Information

ABSTRACT: Colloidal 2D semiconductor nanosheets (NSs) are an interesting new class of materials due to their unique properties. However, synthesis of these NSs is challenging, and synthesis procedures for materials other than the well-known Pb- and Cd-chalcogenides are still underdeveloped. In this paper, we present a new approach to make copper indium sulfide (CIS) NSs and study their structural and optical properties. The CIS NSs form via self-organization and oriented attachment of 2.5 nm chalcopyrite $CuInS_2$ nanocrystals (NCs), yielding triangular- and hexagonal-shaped NSs with a thickness of ∼3 nm and lateral dimensions ranging from 20 to 1000 nm. The self-organization is induced by fast cation extraction, leading to attractive dipolar interactions between the NCs. Primary amines play a crucial role in the formation of the CIS NSs, both by forming *in situ* the cation extracting agent, and by preventing the attachment of NCs to the top and bottom facets of the NSs. Moreover, DFT calculations reveal that the amines are essential to stabilize the covellite crystal structure of the product CIS NSs. The NSs are indium-deficient and the off-stoichiometry gives rise to a plasmon resonance in the NIR spectral window.

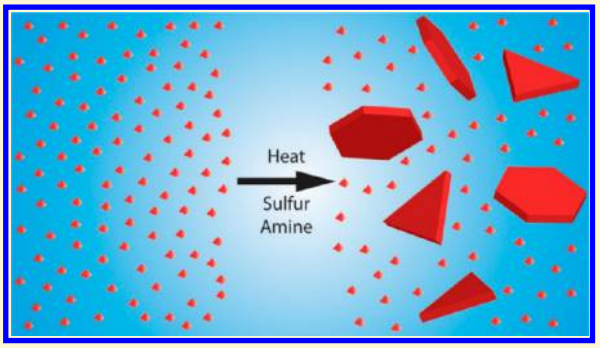

Ultrathin 2-dimensional nanomaterials (nanosheets, NSs) are attracting increasing attention due to their unique physical, electronic, and structural properties.[1−11] Ultrathin colloidal semiconductor NSs with thickness (h) in the strong quantum confinement regime (*i.e.*, $h \leq$ exciton Bohr radius) are of particular interest, since they combine the extraordinary properties of 2D nanomaterials with versatility in terms of composition, size, shape, and surface control, and the prospects of solution processability.[9] To date, colloidal NSs of a variety of binary semiconductors have been prepared: CdX (X = S, Se, Te),[1,6,10] PbS,[2] SnX (X = S, Se),[12,13] InSe,[14] In_2S_3,[15] $Cu_{2-x}S$,[5] $Cu_{2-x}Se$,[16] WS_2,[17,18] and MoS_2.[18] However, reports on NSs of multinary semiconductors are scarce, despite the interesting properties of this class of materials. $CuInS_2$ (CIS) for instance, is a direct semiconductor with a bulk bandgap of 1.5 eV[19,20] and large absorption coefficients,[21] which yields nanocrystals (NCs) with photoluminescence tunable in the vis−NIR (600−1100 nm) spectral range.[22−25]

Size and shape control in a direct synthesis of colloidal multinary NCs is challenging, as the reactivity of three different precursors has to be precisely balanced to prevent formation of the binary system.[24] We circumvented this limitation earlier by a partial Cu^+ for In^{3+} topotactic cation exchange reaction, through which template $Cu_{2-x}S$ NCs are converted into CIS NCs with size and shape preservation.[25−27] A similar cation exchange protocol has been very recently followed by Mu et al.[28] to convert template $Cu_{2-x}S$ NSs[5] into CIS NSs. The two-stage method developed in our work and described in this paper relies on a different mechanism: 2D self-organization of CIS NCs. The resulting 2D NCs have lateral dimensions ranging from 20 nm to 1 μm, thickness of ∼3 nm (similar to the height of the pyramidal-shaped parent NCs), and a Cu:In ratio of ∼3:1, which is different from the 1:1 stoichiometry of the parent CIS NCs. Our results indicate that the self-organization of the parent CIS NCs into 2D NCs and NSs is driven by a sudden change in their composition due to preferential extraction of In^{3+} by *in situ* generated reactive sulfur-containing species (*e.g.*, H_2S). The fast initial growth by oriented attachment of NC building blocks is followed by a slower phase in which NC building blocks are individually added to the edges of the NSs. The crystal structure changes during the reaction from the cubic chalcopyrite structure of the parent CIS NCs to hexagonal covellite. DFT calculations indicate that the ligands play a pivotal role in the formation of the 2D covellite structure and that the In atoms are preferentially located at the surfaces of the NSs. Interestingly, the Cu-rich stoichiometry of the product NSs gives rise to a

Received: November 23, 2017
Published: November 30, 2017

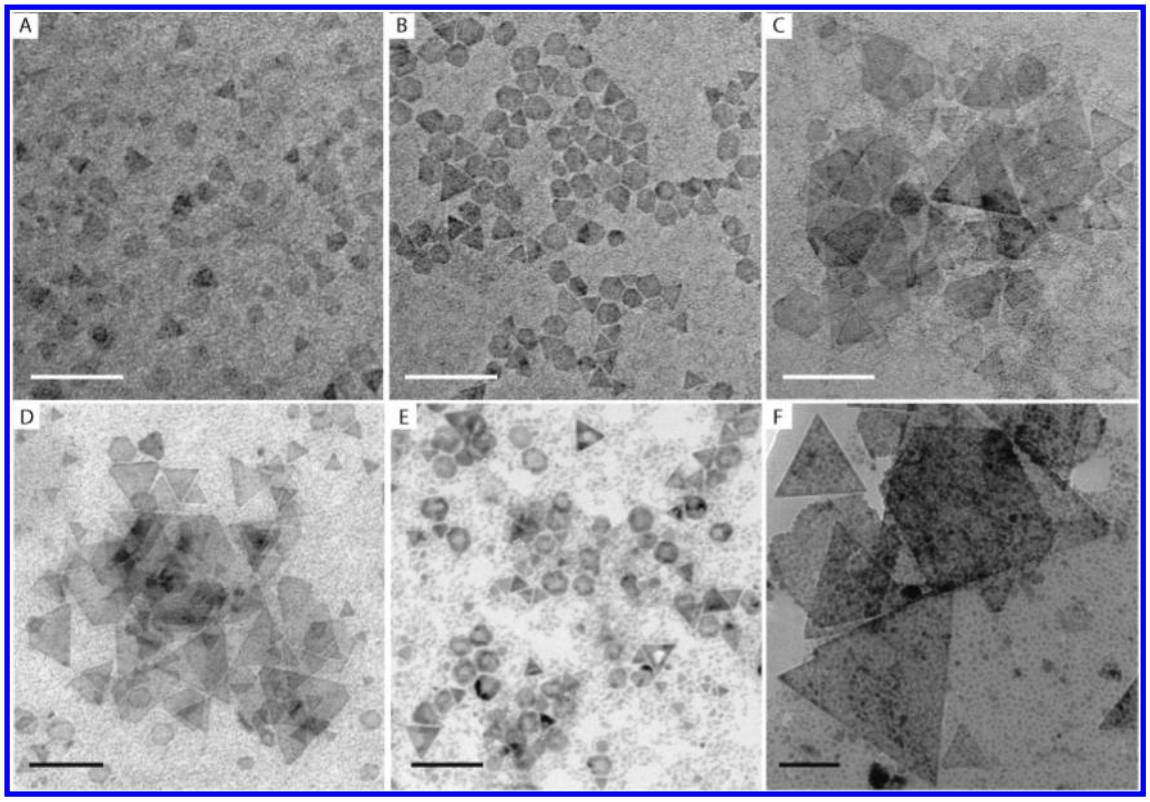

Figure 1. Formation of nanosheets from 2.5 nm parent CIS NCs at 200 °C followed over time with *ex situ* TEM: (A) 1 min, (B) 2 min, (C) 5 min, (D) 1 h, and (E) 5 h of reaction time. (F) Cryo-TEM image of a sample after 2 h at 200 °C. Scale bars correspond to 100 nm.

plasmon resonance in the NIR, making the covellite CIS NSs synthesized in the present work promising materials for plasmonic applications requiring manipulation of NIR light,[29] such as chemical sensing,[29] IR spectroscopy,[29] photothermal therapy,[30] *in vivo* photoacoustic imaging,[31] smart windows,[32] and thermal doping.[33]

EXPERIMENTAL SECTION

Materials. Copper(I) iodide (CuI, Sigma-Aldrich, 98%), indium(III) acetate ($In(Ac)_3$, Sigma-Aldrich, 99.99%), 1-dodecanethiol (DDT, Sigma-Aldrich, ≥98%), sulfur (Sigma-Aldrich, 99.98%), 1-octadecene (ODE, Sigma-Aldrich, technical grade 90%), oleylamine (OLAM, Sigma-Aldrich, technical grade 70%), octadecylamine (ODA, Sigma-Aldrich, technical grade 90%), indium(III) chloride ($InCl_3$, Sigma-Aldrich, 99.999%), zinc(II) chloride ($ZnCl_2$, Sigma-Aldrich, 99.99%), ammonium bromide (Fisher Scientific, +99%), ammonium chloride (Sigma-Aldrich, 99.99%), toluene (Sigma-Aldrich, 99.8%), methanol (Sigma-Aldrich, 99.8%), and butanol (Sigma-Aldrich, 99.8%) were obtained. ODE, OLAM, and ODA were degassed for 2 h at 150 °C before use. All other chemicals were used as received.

$CuInS_2$ Parent Nanocrystal Synthesis. $CuInS_2$ nanocrystals were synthesized following a protocol by Li et al.[34] First, 297 mg of $In(Ac)_3$, 191 mg of CuI, and 5 mL of DDT were mixed and degassed for 1 h under vacuum at 100 °C. The reaction mixture was then heated under N_2 pressure to 230 °C. After 5 min of reaction the heating mantle was removed, and the mixture was allowed to cool down to room temperature (RT). This yields trigonal-pyramidal-shaped CIS NCs with a height of 2.5 nm. The NCs were washed with a methanol/butanol 1/1 mixture, isolated by centrifugation and redispersed in 8 mL of ODE for further reactions or toluene for further analysis.

Nanosheet Synthesis. A 0.4 M stock solution of sulfur dissolved in ODE (S-ODE) was prepared by heating sulfur in ODE to 180 °C until a clear solution was obtained. A 1 mL portion of $CuInS_2$ NCs in ODE (stock solution described above) was mixed with 0.25 mL of OLAM and 0.75 mL of S-ODE in a vial. The vial was then placed in a well in a preheated aluminum block on a hot plate at 200 °C. After 2 h the vial was removed from the aluminum block, and the product NCs were precipitated with a methanol/butanol 1/1 mixture, centrifuged, and redispersed in toluene. For separation of the nanosheets from small nanoparticle byproducts, the dispersion of the product NCs in toluene was left undisturbed for several days at room temperature under N_2 to sediment. Subsequently, the supernatant was carefully removed with a pipet, and toluene was added to the sediment.

In experiments using ODA instead of OLAM, ODA was melted at 60 °C, and then, 0.75 mL was added to the reaction mixture.

In experiments designed to investigate the influence of excess cations in the reaction outcome, 0.0244 g (0.11 mmol) of $InCl_3$ or 0.0252 g (0.11 mmol) of $InCl_3$ and 0.0153 g (0.11 mmol) of $ZnCl_2$ were added to the reaction mixture described above.

In experiments designed to investigate the influence of halide anions, 160.5 mg (3 mmol) of ammonium chloride or 294 mg (3 mmol) of ammonium bromide was added to the reaction mixture described above.

Absorption Spectroscopy. NC solutions in toluene were stored in sealed quartz cuvettes. Absorption spectra were measured on a double-beam PerkinElmer Lambda 950 UV/vis spectrophotometer.

Electron Microscopy. Transmission electron microscopy (TEM), cryogenic TEM, and electron diffraction measurements were performed on an FEI Tecnai-12 microscope. High-resolution transmission electron microscopy and energy dispersive X-ray spectroscopy (EDX) were performed on an FEI TalosF200X microscope. Samples for TEM imaging were prepared by drop-casting a toluene solution containing NCs or nanosheets on a carbon-coated copper grid. Samples for EDX were prepared by drop-casting on a carbon-coated aluminum grid. The sample for cryogenic TEM was prepared using an FEI Vitrobot instrument. The electron diffraction patterns were first radially integrated using the CrystTBox toolbox.[35] The pattern obtained was scaled with a scaling factor determined by fitting a measured gold reference electron diffraction pattern to a gold reference signal.

DOI: 10.1021/acs.chemmater.7b04925
Chem. Mater. 2017, 29, 10551−10560

DFT Calculations. The binary Cu−S system has a very rich phase diagram, with a variety of equilibrium compositions and crystal structures, ranging from chalcocite Cu_2S to covellite CuS.[24] Calculations were carried out for the CuS composition because the CIS NSs synthesized in the present work were observed to have adopted the covellite crystal structure. The phase diagram of the binary In−S system is also very rich, and therefore the 1:1 stoichiometry was chosen to allow a direct comparison with covellite CuS. The calculations of CIS bulk structures and bare CIS slabs were performed using the plane augmented wave (PAW) method[36] with the generalized gradient approximation (GGA) of Perdew−Burke−Ernzerhof (PBE)[37] as implemented in the Vienna *ab initio* simulation package (VASP) code.[38,39] The cutoff energies for the wave functions and augmentation functions were set to 550 and 770 eV, respectively, and sufficiently dense *k*-meshes were used to ascertain energy convergence to within 2 meV/atom. This resulted in *k*-meshes of 14 × 14 × 4 for the covellite structure, 6 × 6 × 4 for 2 × 2 × 1 supercells of the covellite structure, 14 × 14 × 8 for the chalcopyrite structure, and 16 × 8 × 18 for the orthorhombic InS structure.[40] Both the crystal lattice and the atomic coordinates were fully relaxed. The formation enthalpy is defined with respect to pure CuS covellite and pure InS covellite as

$$\Delta E^{\text{form}}(Cu_{1-x}In_xS) = E(Cu_{1-x}In_xS) - (1-x)E(CuS)^{\text{cov}} - xE(InS)^{\text{cov}} \quad (1)$$

For ligand-covered configurations, supercells were constructed that were 58 Å in height, containing a vacuum slab at least 22 Å thick. Only for these configurations, the OptB88-vdW functional by Dion, as implemented in the VASP code by Klimeš et al.,[41] was used to take into account van der Waals interactions. After full relaxation (dimensions and atomic coordinates) the lateral cell dimensions were kept fixed for evaluation of the ligand coverage using OptB88-vdW while allowing full relaxation of atomic coordinates.

RESULTS AND DISCUSSION

Briefly, the nanosheets (NSs) are synthesized by suspending dodecanethiol-capped chalcopyrite CIS NCs in a solution of elemental sulfur in octadecene and a primary amine (octadecylamine or oleylamine, OLAM), and subsequently heating the mixture to 200 °C (see the Experimental Section for details). This induces the formation of triangular and hexagonal NSs at the expenses of the parent CIS NCs (Figure 1). Interestingly, the NSs only form when both sulfur and a primary amine (either octadecylamine or OLAM) are present (Supporting Information, Figure S1). Elemental sulfur has been previously shown to react with alkylamines forming alkylammonium polysulfides at room temperature, and alkylthioamides, dialkylamidines, alkyl-thioketoamidines, and H_2S at elevated temperatures (<100 °C).[42] Under appropriate conditions the released H_2S was shown to readily combine with metal precursors present in the reaction medium to form metal sulfide NCs.[42] In a control experiment (Supporting Information, Figure S2) we show that H_2S is also formed under the conditions used in our NS synthesis method. This implies that H_2S (or another product of the reaction between OLAM/ODA and sulfur) is crucial to trigger the conversion of the parent CIS NCs into the product NSs. A mechanism for this transformation will be proposed later in this paper. Figure 1A shows that after 1 min at 200 °C the NSs have already grown to 25 ± 4 nm in lateral size, which is 10 times larger than the parent CIS NCs (trigonal-pyramidal-shaped with a base of 2.5 nm and height of 2.4 nm).[23] Nanosheets also form at lower temperatures (*e.g.*, 80 °C, Figure S3; or even at room temperature, Figure S4), but the growth kinetics are much slower. The NS thickness is determined to be 3−4 nm by analyzing TEM images of NS stacks (Figure S5).

The growth of the NSs at 200 °C was followed *ex situ* with TEM. Over time, both the lateral dimensions and the polydispersity of the NSs increase, with sizes ranging from tens to several hundreds of nanometers after 1 h of reaction (Figure 1A−D). Interestingly, most of the growth occurs in the first 5 min. If the reaction is allowed to continue for several hours, the NSs start to shrink and break down (Figure 1E). Small irregularly shaped nanoparticles, with sizes ranging from 4 to 11 nm, are observed to coexist with the nanosheets at all times (Figure 1 and Figure S6). Cryo-TEM (Figure 1F) shows that these small nanoparticles are present both as free-standing particles in solution and as adsorbates attached to the nanosheet surface. Most importantly, the cryo-TEM images also clearly demonstrate that the NSs are already present in the reaction medium, thereby excluding the possibility that they are formed on the TEM grid by drying effects or electron-beam-induced aggregation.

Elemental Composition of the NSs. The formation of nanosheets at 200 °C was also followed over time with *ex situ* absorption spectroscopy (Figure 2). The parent CIS NCs show

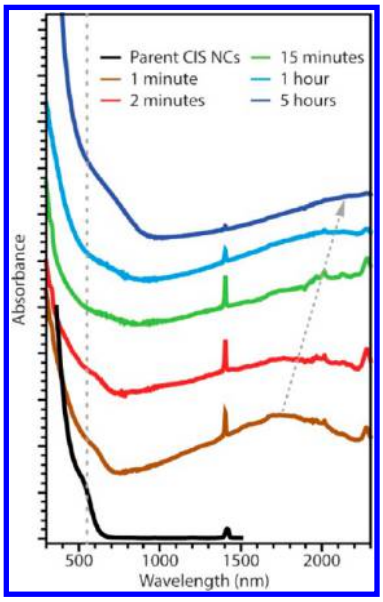

Figure 2. Absorption spectra of the parent CIS NCs (black) and the product CIS NSs at different stages of the reaction. The dashed line at ~550 nm marks the position of the band-edge absorption transition of the parent NCs, while the dashed arrow highlights the shift of the broad NIR absorption band to lower energies over time. It is noted that this band is absent in the spectrum of the parent NCs. The sharp peak at 1400 nm is due to residual methanol, which was used to wash the samples.

a rather featureless absorption spectrum extending to ~650 nm with a shoulder at ~550 nm, which is ascribed to the band-edge (1S−1S) transition.[23] This shoulder broadens and shifts to longer wavelengths as the reaction proceeds, indicating a reduction in the bandgap of the NCs, which is consistent with a decrease in the quantum confinement as a result of the growth of the nanosheets. Furthermore, an additional broad absorption band appears in the near-infrared (NIR) region, which further broadens and shifts to longer wavelengths over time (see Figure 2; peak is at 1700, 2000, and 2200 nm for the 1 min, 1 h, and 5 h samples, respectively). A (strong) absorption band in the NIR

DOI: 10.1021/acs.chemmater.7b04925
Chem. Mater. 2017, 29, 10551−10560

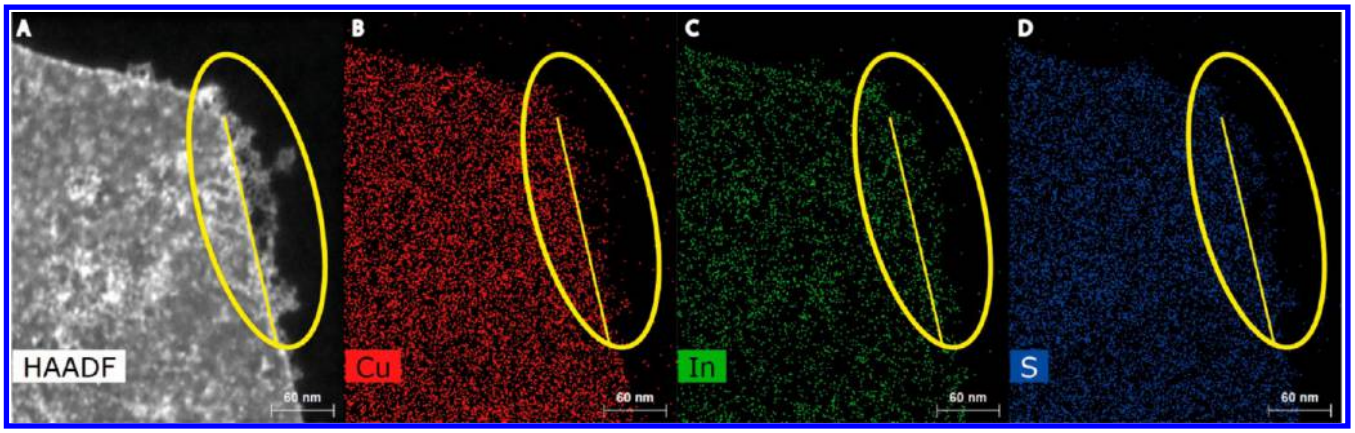

Figure 3. (B, C, D) STEM-EDX elemental maps of the nanosheet shown in the STEM-HAADF image in part A. The yellow frame highlights a region where clusters of small nanoparticles are observed at the edge of the nanosheet. The diagonal yellow line marks the edge of the nanosheet. The nanoparticles appear brighter in the In map than in the Cu map, suggesting that they are In-rich CIS. This is clearer visible in the close-up of this image in the Supporting Information, Figure S8.

is often observed in Cu-chalcogenide NCs and is ascribed to a localized surface plasmon resonance (LSPR) due to excess charge carriers.[24,29] These excess charge carriers are present because of stoichiometry deviations, typically Cu-vacancies, which lead to excess holes in the valence band (*i.e.*, p-doping).[24,29] The observation of a strong NIR absorption band in the spectra of the product CIS NSs thus implies the presence of excess carriers, suggesting that the NSs no longer have the 1:1 Cu:In stoichiometry of the parent CIS NCs.

Indeed, energy-dispersive X-ray spectroscopy (EDX) on wide areas, encompassing a large ensemble of NSs, reveals that the average elemental composition of the nanosheets is Cu/In/S 0.6(±0.01):0.3(±0.004):1 (see the Supporting Information, Figure S7, for a representative example), which is clearly different from the 0.5:0.5:1 stoichiometry of the parent CIS NCs, suggesting that, to keep charge neutrality, (part of) the sulfur ions formed covalent bonds, similarly to the CuS covellite phase.[43] This should result in excess holes in the valence band, giving rise to an LSPR, consistent with the NIR absorption band observed in the spectra of the NSs (Figure 2). Elemental analysis of individual NSs (Figure 3 and Figure S8) reveals small variations within a sample: The average Cu:In ratio of 11 measured nanosheets is 1:0.3 ± 0.06. The highest Cu:In ratio is 1:0.39, while the lowest is 1:0.21. Additionally, the small NCs seem to be In-rich CIS, as they appear brighter in the In map than in the Cu map (see Figure 3 and Supporting Information, Figure S8). The elemental maps provide no evidence for the formation of In_xS_y NCs, since all regions examined contained both Cu and In, albeit in different ratios (*i.e.*, NSs are Cu-rich, NPs are In-rich). The difference between the average Cu:In ratio determined for the NS ensemble (*viz.*, 2:1) and for individual NSs (*viz.*, 3:1) can be ascribed to the fact that the contribution of the In-rich NCs is much larger in the ensemble measurements. The average composition of the NSs at different stages of the reaction was also analyzed with EDX and observed to be essentially constant. This shows that the cation extraction is fast and is, in fact, already completed within the first minute of the reaction. This observation also indicates that the shift of the NIR LSPR absorption band during the reaction (Figure 2) is due to the lateral growth of the nanosheets, rather than a change in their composition. The consequences of these observations for the proposed formation mechanism will be discussed below. It should be noted that the LSPR band originates from the In-poor NSs, rather than from the In-rich CIS NCs. This becomes evident when comparing the absorption spectrum of a sample of NSs obtained by sedimentation with that of the original ensemble prior to sedimentation, when a high concentration of small In-rich NCs was still present (Figure S9). The LSPR band is very pronounced in the absorption spectrum of the sample obtained by sedimentation, but is hardly observable in the spectrum of the sample prior to sedimentation, which is dominated by the absorption of the small In-rich NCs.

Shape of the NSs. As shown in Figure 1 (and also in Figures S1D, S6, and S8) the shape of the nanosheets ranges from triangles to hexagons, through truncated triangles and irregular hexagons. Remarkably, the NS edges are often kinked and irregular (see Figure 4A,B and also Figures S6 and S8A). Figure 4B also clearly shows small particles adsorbed on the nanosheets' surface. Moreover, the edges of the NS in Figure 4B are noticeably brighter than its interior, suggesting that the edges are richer in indium. This observation is consistent with the structural model derived from DFT calculations and will be discussed in more detail below. The high-resolution TEM (HR-TEM) image in Figure 4C shows lattice fringes of small particles on the nanosheet surface and the nanosheet itself. It is clear that the fringes have different directions, indicating that the small particles have different orientations on the surface and are not atomically aligned with the underlying nanosheet. The wobbly edge of the NS in Figure 4C is deformation caused by the intense electron beam. This deformation happens *in situ* while imaging the NS and worsens over time. The implications of the irregularities and kinks observed in the edges of the NSs in the low-resolution TEM images will be discussed in the mechanism section below.

Crystal Structure of the NSs. Electron microscopy was also used to study the crystal structure of the nanosheets, by using selected area electron diffraction (SAED) and comparing the integrated pattern to bulk reference patterns. Figure 5A shows the SAED pattern of a batch of nanosheets on the TEM grid. Azimuthal integration of the SAED pattern yields the signal shown in Figure 5B, which is in good agreement with a covellite bulk reference pattern. The SAED pattern of a single NS (Figure 5C,D) shows diffraction spots consistent with a single crystal. The hexagonal pattern can be indexed to covellite lattice planes (Figure S11). The crystallographic properties of

DOI: 10.1021/acs.chemmater.7b04925
Chem. Mater. 2017, 29, 10551−10560

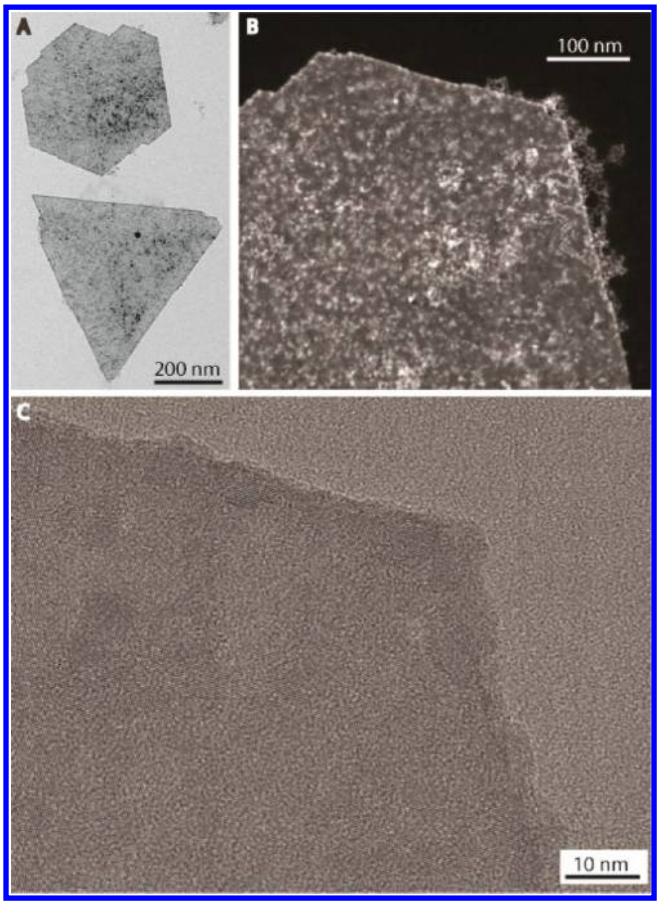

Figure 4. (A) TEM image showing kinked and irregular edges of NSs. (B) STEM-HAADF image showing kinked edges and small particles adsorbed on the surface and at the edges of a NS. (C) HR-TEM image showing lattice fringes of both the nanosheet and small particles adsorbed on the nanosheet surface in different orientations.

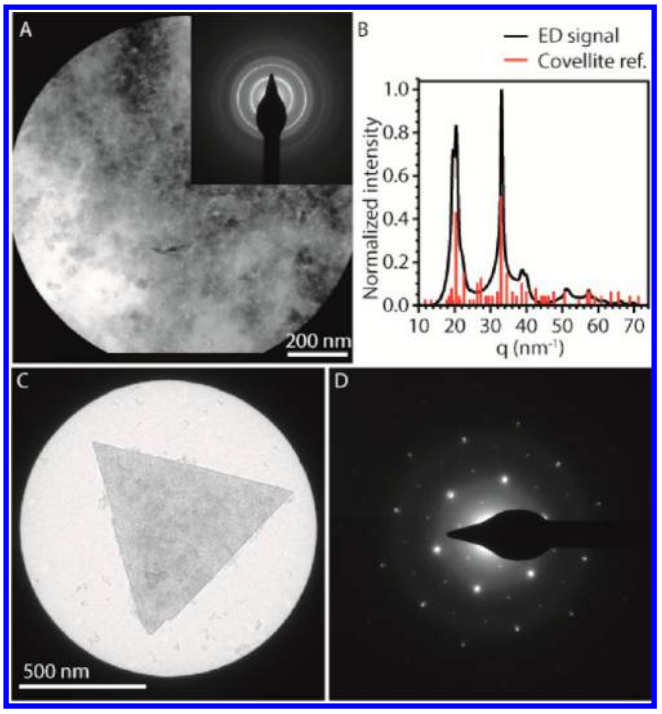

Figure 5. (A) Selected area showing a batch of deposited nanosheets. The electron diffraction pattern of this batch is shown in the inset. A larger version of this panel is shown in Figure S10. (B) Azimuthally integrated SAED signal is compared to a covellite bulk reference pattern (JCPDS PDF card 00-036-0380). SAED of (C) a single nanosheet shows (D) a hexagonal diffraction pattern.

the product CIS NSs are further studied with DFT calculations below.

DFT Modeling of Crystal Structures. During the reaction, the 2.5 nm parent CIS NCs, with chalcopyrite crystal structure, transform to NSs with much larger (~100-fold) lateral dimensions and covellite crystal structure. For insight into the energetics of the crystallographic transformation from chalcopyrite to covellite, plane-wave density functional theory (DFT) calculations were performed using the plane augmented wave (PAW) method with the generalized gradient approximation (GGA) as implemented in the VASP code.[38,39] Computational details are given in the Experimental Section. The calculations, over the entire cation range but limited to compositions with a cation/anion ratio of one, were performed both for the CuS-type covellite structure and for the $CuInS_2$-type chalcopyrite structure displayed in Figure 6A,B. Also the known most stable orthorhombic phase of InS shown in Figure 6C was considered. The formation enthalpies, defined with respect to CuS covellite and InS covellite (see the Experimental Section for details), are shown in Figure 7. Tangent lines are drawn connecting the most stable covellite phases, and the overall most stable phases. The total-energy calculations confirm that covellite CuS, chalcopyrite $CuInS_2$, and orthorhombic InS are overall the energetically most stable phases. In the compositional range of $Cu_{1-x}In_xS$ with x between 0.5 and 1.0, phase separation into chalcopyrite $CuInS_2$ and orthorhombic InS is predicted. For the experiments, only the compositional range with In concentrations between 0.0 and 0.5 is relevant. The DFT calculations show that the chalcopyrite structure is more stable over this compositional range, except for In concentrations below $x \sim 0.05$ where the CuS covellite structure is more stable. At an In concentration of $x \sim 0.25$ (corresponding to the experimentally determined composition of the nanosheets), the tangent line connecting the most stable covellite phases and the tangent line connecting the most stable chalcopyrite phases are very close, with a formation enthalpy difference of only 104 meV per formula unit (fu). The fact that the covellite structure is found experimentally shows that the ligands, which are not included in these bulk calculations, are required to stabilize the covellite phases with a nonzero In content, thereby bridging this difference in formation enthalpy.

As can be seen in Figure 7, there are multiple data points for the formation enthalpies of the covellite phases (black circles) at one particular composition. This is because multiple orderings of the Cu/In atoms inside the (Cu, In)S covellite structure were considered, varying from concentrating In atoms in particular layers to a more homogeneous distribution in the structure. From all of these calculations, it can be concluded that it is remarkable that the covellite structure is found experimentally, as—at least for bulk phases—the covellite structure cannot accommodate large concentrations of In atoms without severe distortion. The covellite crystal structure is characterized by triplets of CuS atomic planes (Figure 6A) that are bonded by S−S bonds oriented perpendicular to the layered structure. The central CuS atomic layer in the triplets is atomically flat. However, upon introduction of In atoms in the structure, in general this central layer becomes buckled as shown in Figure 6E. It is noted that, in the chalcopyrite

DOI: 10.1021/acs.chemmater.7b04925
Chem. Mater. 2017, 29, 10551−10560

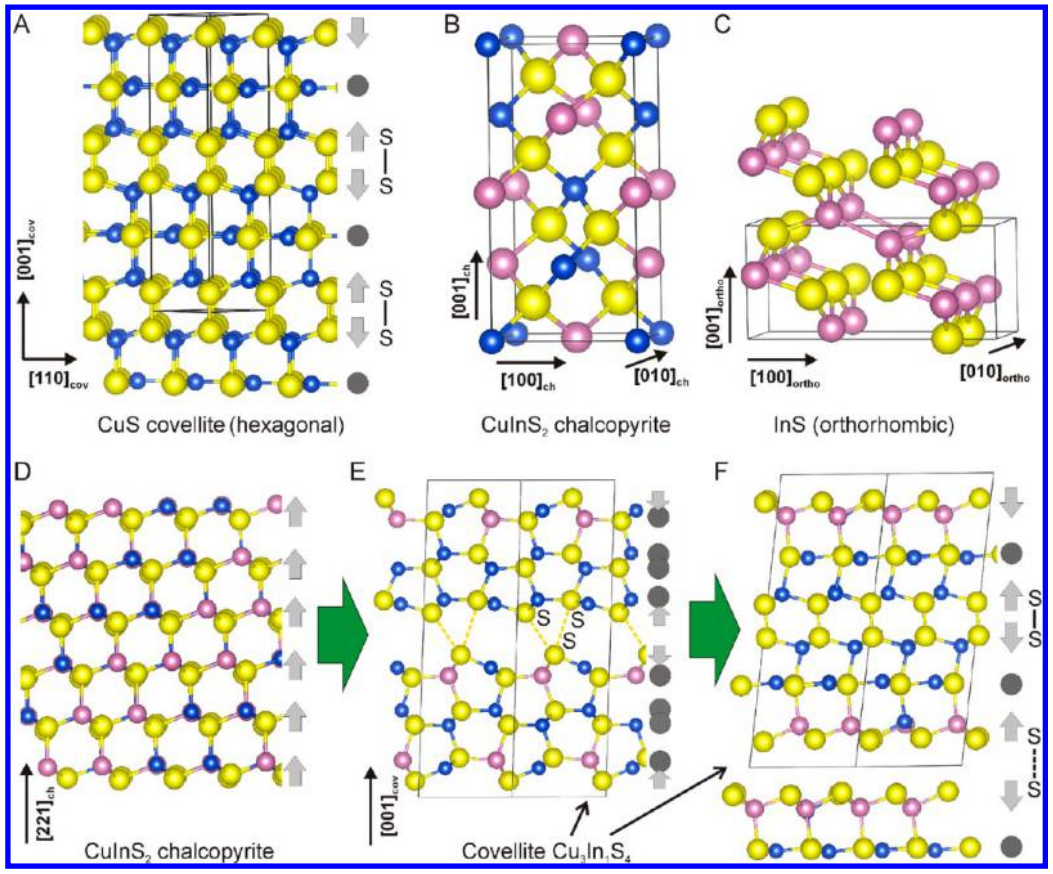

Figure 6. Schematic bulk crystal structures of (A) covellite, (B) chalcopyrite, and (C) orthorhombic InS. Cu atoms are displayed in blue, In atoms in magenta, and S atoms in yellow. The simulation cells are periodic in all dimensions and are drawn with black lines. (D–F) Proposed transformation sequence from chalcopyrite to covellite, with projections corresponding to side views of the NSs. Gray arrows drawn at the right-hand side of panels A, D, E, and F indicate the directionality of bilayers, pointing from anion-filled atomic layers to cation-filled atomic layers. Gray dots indicate atomic layers filled with both anions and cations. The {112} atomic planes of the (D) chalcopyrite structure consist of hexagonal (Cu, In)S_2 bilayers which we draw aligned with the {001} planes of the (E, F) covellite superstructure. Upon extraction of In atoms, the Cu atoms occupy the vacant sites, and reordering causes the cation–anion separated bilayers to become (E) mixed atomic layers, thereby providing opportunities for S–S bond formation. Further atomic rearrangements result in structure F, with oppositely directed bilayers that are typical of the covellite structure. This last structure is predicted to be the lowest-energy covellite $Cu_3In_1S_4$ phase.

structure, the directionality of the anion–cation bilayers is uniform in the $[221]_{ch}$ direction, as indicated with the gray arrows in Figure 6D. In the covellite structure of Figure 6A, though, the bilayers show opposing directionality in the corresponding $[001]_{cov}$ direction (also indicated with gray arrows). Figure 6E is therefore an intermediate structure, where the bilayers do not consist of an anion-filled atomic plane and a cation-filled atomic plane, but of cation–anion mixed layers. The energetically most favorable orderings in the covellite structures were those whereby the In atoms occupy the atomic planes adjacent to the S–S bonds, as shown in Figure 6F. However, this also leads to strong weakening of the S–S bonds at particular planes, with the interatomic S–S distance increasing substantially from 1.7 Å for pure CuS (Figure 6A) to ~3.0 Å for the S atomic layers shown at the bottom of Figure 6F. In addition, these In-coordinated S layers adopt a more conventional stacking. The large interatomic distances suggest that, along these planes, the structure could be more easily cleaved or layers exfoliated; *i.e.*, surfaces will be formed more easily at these lattice planes.

Although the dynamics of the transformation sequence (with cation extraction, ligand replacement, and oriented attachment all taking place over a very short time window) is much too complex to be resolved by means of total-energy DFT calculations, the calculations point to a plausible transformation pathway which is shown in Figure 6D–F. The {112} atomic layers of $CuInS_2$ chalcopyrite show structural resemblance to the (001) layers of (Cu, In)S covellite. Starting from the chalcopyrite structure (Figure 6D), In extraction provides flexibility in the atomic environments, allowing the Cu(I)-sublattice to quickly reorganize itself by occupation of the vacant sites. This results in mixed anion–cation bilayers in the {112} chalcopyrite planes, which then transform into {100} covellite planes (Figure 6E). This process is likely favored by the very high solid-state mobility of Cu(I) cations in chalcogenide lattices.[25−28,44] Such a transformation can also be much enhanced when chalcopyrite NCs come in a direct solid–solid contact with a larger covellite nanosheet by means of directed attachment. As a result, layered structures are formed that are terminated with S atoms at both sides so that S–S bonds can be formed. Next, atomic rearrangements take place whereby In atoms become concentrated near S–S bonded planes, which enables the formation of the nearly flat CuS atomic planes at the center of the triplet layers that are so typical of the covellite structure (Figure 6A). Because of the strong S–S bonds in the case of a Cu-rich atomic environment and the weak S–S bonds in the case of an In-rich environment (both shown in Figure 6F), we hypothesize that the interior of

DOI: 10.1021/acs.chemmater.7b04925
Chem. Mater. 2017, 29, 10551–10560

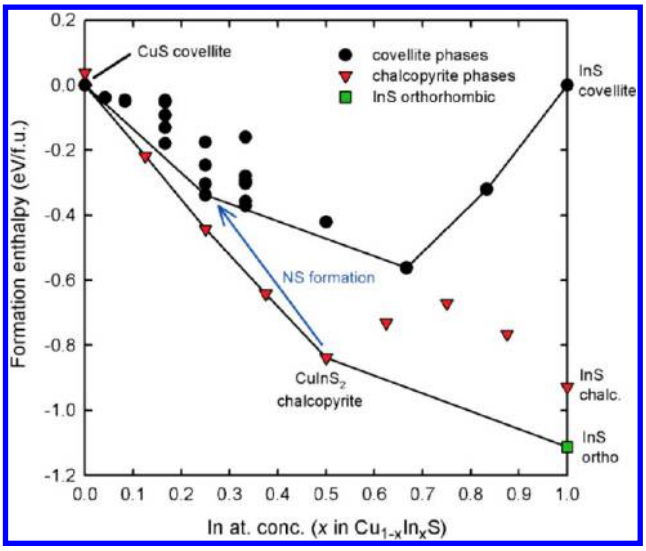

Figure 7. Formation enthalpies of $Cu_{1-x}In_xS$ bulk phases, relative to CuS covellite and InS covellite, calculated using GGA–PBE. The covellite phases are indicated by black circles, chalcopyrite phases by red triangles, and the orthorhombic InS phase by a green square. The top black line is the common tangent connecting the most stable covellite phases; the bottom black line is the common tangent line connecting the overall most stable phases. The blue arrow indicates the change induced by the NS formation reaction.

the covellite NSs are Cu-rich, while the surfaces of the NSs are In-rich, and that these InS-terminated surfaces preferably bind to ligands.

Calculations were also performed on a 6-bilayer slab of the chalcopyrite structure, and a 6-bilayer slab of the covellite structure (both at In concentration $x = {}^1/_3$). Upon comparison of the formation enthalpies of bare {001} covellite CIS NSs with bare {112} chalcopyrite CIS NSs, it was found that the chalcopyrite NSs are energetically slightly more favorable by 57 meV/fu. Therefore, the DFT calculations predict that the 2D covellite structure cannot be stabilized by surface energies alone, and that the ligands likely play a pivotal role in stabilizing the colloidal 2D CIS covellite phase. Additional simulations were performed in which 6-bilayer covellite slabs were covered with amine or thiol ligands. To take into account van der Waals interactions, these calculations were performed with the computationally more expensive OptB88-vdW functional instead of the GGA–PBE functional (details in the Experimental Section). Figure S12 shows the configurations found for bare, crystal-bound thiol-covered, surface-bound thiol-covered, and amine-covered 2D CIS covellite slabs. We note here that not all possible terminations of the CIS covellite structure (Cu, In orderings) were simulated, neither were different ligand areal densities, as this configurational space is too large to be explored with quantum mechanical DFT calculations. As the end groups mainly determine the interaction with the 2D slabs, for computational efficiency only 6-carbon-atom-chain variants of the ligands (*i.e.*, the C_6H_{13} hexyl radical, the $C_6H_{13}S$ thiyl radical, and $C_6H_{15}N$ hexylamine) were considered. Not surprisingly, all ligands were found to have a favorable binding energy with the CIS nanosheets when taking the energies of the bare nanosheets and of the ligand 2D layers as a reference. However, in the thiol-covered configurations of Figure S12B,C, the remaining forces on the atoms are very high (up to 0.7 and 1.0 eV/Å for the crystal-bound and surface-bound configurations, respectively) rendering thiol coverage unlikely, while the amine-covered configuration displayed in Figure S12D relaxed well, with forces on the atoms on average 0.03 eV/Å and at most 0.09 eV/Å. Therefore, the DFT calculations indicate that OLAM coverage is preferred over DDT coverage of the covellite CIS nanosheets. It is thus likely that the formation of covellite (rather than chalcopyrite) CIS nanosheets was driven by the presence of large concentrations of OLAM (or other alkylamines) in the reaction medium.

Cation Extraction. As shown above, the nanosheets are indium-poor, and the final stoichiometry is already reached after 1 min of reaction. The DFT calculations discussed above imply that the extraction of In from the parent CIS NCs is crucial to initiate the transformation from the chalcopyrite to the covellite structure, which, in the presence of OLAM ligands, can form stable In-poor CIS nanosheets. For verification of whether the extraction of indium is indeed essential for the formation of the CIS nanosheets and whether the final composition of the product NSs can be controlled, cation precursor salts were added to the reaction mixture. Both $InCl_3$ and $ZnCl_2$ were added, and in both cases nanosheets were not formed (Figure S13A,B). In contrast, addition of ammonium halides (chloride and bromide) to the reaction mixtures had no impact on the formation of the nanosheets (Figure S13C,D). This confirms that extraction of In(III) cations from the parent CIS NCs (which is prevented when excess In(III) and Zn(II) cations are present) is essential for the formation of nanosheets.

Formation Mechanism of the CIS Nanosheets. Several mechanisms have been proposed in the literature for the formation of two-dimensional (2D) colloidal semiconductor NCs.[1,2,5,9,10,13−18,45−48] These mechanisms can be roughly divided into three different categories:[9] (i) 2D anisotropic growth by monomer addition to specific crystallographic facets (CdS,[1] CdSe,[1,6,47,48] WS_2,[17,18] MoS_2[18]); (ii) self-organization by 2D-oriented attachment of NC building blocks (PbS,[2] SnSe,[13] In_2S_3,[15] $Cu_{2-x}Se$,[16] CdTe[49−51]); and (iii) 2D-constrained growth within soft lamellar templates ($Cu_{2-x}S$,[5] CdS,[10] CdSe,[10] InSe,[14] PbS[46]). These mechanisms have been recently discussed in detail,[9] so we will here only highlight their essential aspects. In the first mechanism, monomers (*i.e.*, molecular [MX] units) formed upon reaction between M- and X-precursors attach to specific crystallographic facets of a growing NC (or a magic-size cluster) resulting in 2D anisotropic growth. The 2D constraints in this mechanism are attributed either to selective capping of the top and bottom facets with suitable ligands,[6,47] or to higher activation energies for monomer addition on the large top and bottom facets.[48] In the self-organization mechanism the 2D geometry of the resulting NC superlattice is ascribed to oriented attachment due to both directional (dipolar) interactions between specific high-free-energy facets[2,49−51] and dense ligand layers on the facets perpendicular to the attachment plane.[2,16] In the soft-template mechanism, the nanosheets form within pre-existing 2D lamellar templates consisting of dense self-assembled monolayers of linear alkyl chain ligands, metal cations, and small anions (such as halides),[10,14,45,46] which impose 2D constraints on growth by both monomer addition to NC nuclei[14,45,46] and self-organization of NC (or magic-size cluster) building blocks.[10]

The mechanism we propose here for the formation of In-poor covellite CIS nanosheets from parent chalcopyrite $CuInS_2$ NCs is based on 2D self-organization of *in situ* produced NC building blocks, followed by fusion and recrystallization (Figure

DOI: 10.1021/acs.chemmater.7b04925
Chem. Mater. 2017, 29, 10551−10560

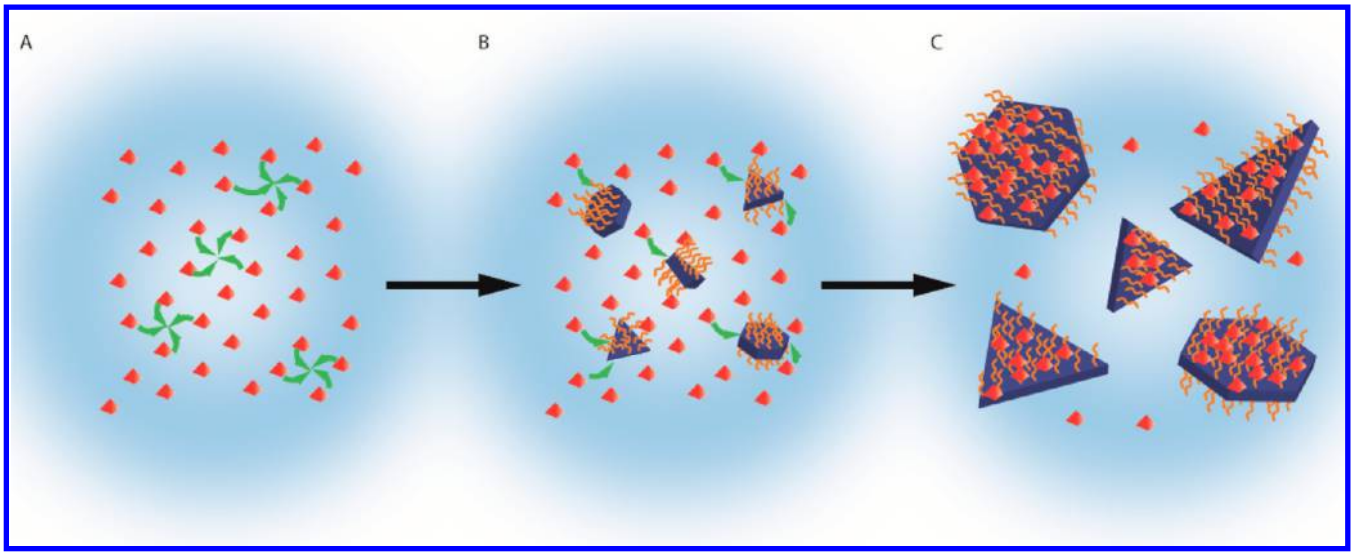

Figure 8. Schematic representation of the proposed formation mechanism for the In-poor CIS NSs. (A) The first step is the extraction of In from the parent chalcopyrite CIS NCs, which induces a fast initial growth by oriented attachment of In-poor CIS NC building blocks, followed by fusion and recrystallization into single-crystalline covellite NSs. (B) Subsequent growth occurs by addition of CIS NC units to the side facets of the NSs. (C) The NS growth stops when the parent (In-poor) CIS NCs (*i.e.*, "monomers") in the reaction medium have been almost completely depleted.

8). The first step, completed within the first minute of the reaction, consists of a fast extraction of indium by reactive sulfur-containing species formed *in situ* upon reaction between elemental sulfur and OLAM or ODA (probably H_2S, which is the most reactive of the *in situ* generated species).[42] This sudden change in composition most likely leads to drastic modifications in the free energies and charge distributions of the different crystallographic facets of the parent pyramidal chalcopyrite CIS NCs, thereby inducing dipolar interactions between the NCs, similarly to previous observations on tetrahedral zinc-blende CdTe NCs that had been subjected to reactions changing the surface composition of the NCs.[49−51] We propose that these dipolar interactions between the In-poor CIS NCs lead to their fast self-organization into 2D NSs by oriented attachment driven by minimization of the imbalanced surface free energies (Figure 8A). On the basis of the DFT calculations discussed above, it is likely that the oriented attachment process is accompanied by a fast ligand-assisted structural reorganization through which the In-poor CIS NC superlattice fuses and transforms into single-crystalline OLAM-capped In-poor covellite CIS nanosheets. The OLAM ligands not only are crucial to stabilize the In-poor covellite CIS phase (see DFT calculations above), but also play an important adjuvant role in directing the 2D self-organization, both by stabilizing the top and bottom facets of the nanosheets and by preventing attachment of NC building blocks on them, thereby constraining the growth to the lateral directions only, as has been observed in other systems.[2] This is clearly illustrated by the observation of randomly oriented small nanoparticles adsorbed on the NS surface, without fusing to it (see, *e.g.*, Figures 1F, 3, and 4). It should be noted that the reaction between elemental sulfur and alkylamines produces a number of species that can also function as ligands (*viz.*, alkylthioamides, alkyl-thioketoamidines, dialkylamidines).[42] However, these molecules either are bulkier than OLAM (or ODA) or contain a thiol donor group, which, according to the DFT calculations discussed above, should lead to less effective stabilization of the NS surfaces as compared to OLAM.

The initial fast growth by self-organization is a multibody event in which several NCs must collide to form a 2D superstructure. This process can only be sustained if the concentration of NC building blocks is sufficiently high. At low concentrations of parent NCs, growth can only proceed by sequential addition of individual In-poor CIS NCs to the edges of the NSs, in a process that is equivalent to NC growth by monomer addition[52] (Figure 8B, the NCs are the "monomers"). This results in the kinked and ragged edges observed in many of the NSs (*e.g.*, Figures 1F and 4, and Figure S6). Again, the ligands prevent the incorporation of NCs through addition to the bottom and top facets of the nanosheets. The concentration of available In-poor NC building blocks (*i.e.*, free in the reaction medium) eventually decreases below a critical limit, causing the growth of the NSs to stop (Figure 8C). We note that, as discussed above, the NCs observed simultaneously with the NSs (either attached to their edges and surfaces, or dispersed throughout the TEM grid) are In-rich, and are thus unlikely to be leftover building blocks of the In-poor NSs. We propose that these In-rich NCs are byproducts of the reaction that induces the formation of the NSs, being formed by incorporation of the In(III) extracted from other CIS NCs. This process establishes a partition of the initial ensemble of parent 2.5 nm CIS NCs into 2.5 nm In-poor CIS NCs (which become the nanosheet building blocks) and larger than 2.5 nm (due to incorporation of "InS" units) In-rich NCs that remain as isolated NCs. We note that CIS NCs are very tolerant to stoichiometry deviations and can be readily made with Cu:In ratios ranging from 0.3 to 2.9.[24] Interestingly, the oxidation state of Cu and In in $Cu_xIn_yS_z$ is the same in all compositions (*i.e.*, +1 and +3, respectively) because the neutrality of the NCs is ensured by the change in the formal oxidation state of the sulfur atoms, leading to excess carriers in either the valence or the conduction bands. As discussed above, this is consistent with the observation of LSPR bands in the absorption spectra of the covellite CIS NSs.

DOI: 10.1021/acs.chemmater.7b04925
Chem. Mater. 2017, 29, 10551−10560

CONCLUSIONS

Colloidal indium-deficient covellite CIS nanosheets (NSs) with a thickness of ∼3 nm and lateral dimensions up to 1 μm were obtained via a two-stage synthetic procedure, in which pyramidal chalcopyrite $CuInS_2$ NCs (height, 2.5 nm) were used as parent NCs. Fast indium extraction by *in situ* generated reactive sulfur species (*e.g.*, H_2S) triggers a rapid self-organization and oriented attachment process that is accompanied by fusion and recrystallization of the In-poor CIS NC building blocks, yielding single-crystalline covellite CIS NSs. Further growth occurs by addition of individual In-poor CIS NCs to the side facets of the NSs, until the NC building blocks available for growth are depleted. Alkylamine ligands (OLAM or ODA) are essential for the formation of the NSs both because they are required for the *in situ* generation of the cation extraction agent from elemental sulfur and because they play a pivotal role in stabilizing the In-poor covellite structure and in directing the 2D anisotropic growth by preventing addition of NC building blocks to the top and bottom facets of the NSs. The Cu-rich stoichiometry of the product CIS NSs gives rise to a plasmon resonance in the NIR, making them promising materials for plasmonic applications.[29−33]

ASSOCIATED CONTENT

Supporting Information

The Supporting Information is available free of charge on the ACS Publications website at DOI: 10.1021/acs.chemmater.7b04925.

TEM images, description of H_2S formation experiment, EDX spectra, additional elemental maps, diffraction spots, and image showing ligand coverage of different surfaces as determined with DFT (PDF)

AUTHOR INFORMATION

Corresponding Author

*E-mail: c.demello-donega@uu.nl.

ORCID

Marijn A. van Huis: 0000-0002-8039-2256

Celso de Mello Donega: 0000-0002-4403-3627

Author Contributions

The manuscript was written through contributions of all authors. All authors have given approval to the final version of the manuscript.

Notes

The authors declare no competing financial interest.

ACKNOWLEDGMENTS

A.C.B. and C.d.M.D. acknowledge financial support from the division of Chemical Sciences (CW) of The Netherlands Organization for Scientific Research (NWO) under Grant ECHO.712.014.001. M.A.v.H. acknowledges financial support from the European Research Council (ERC-CoG, Grant 683076).

REFERENCES

(1) Ithurria, S.; Tessier, M. D.; Mahler, B.; Lobo, R. P. S. M.; Dubertret, B.; Efros, A. L. Colloidal Nanoplatelets with Two-Dimensional Electronic Structure. *Nat. Mater.* **2011**, *10*, 936−941.

(2) Schliehe, C.; Juarez, B. H.; Pelletier, M.; Jander, S.; Greshnykh, D.; Nagel, M.; Meyer, A.; Foerster, S.; Kornowski, A.; Klinke, C.; et al. Ultrathin PbS Sheets by Two-Dimensional Oriented Attachment. *Science* **2010**, *329*, 550−553.

(3) Rao, C. N. R.; Ramakrishna Matte, H. S. S.; Maitra, U. Graphene Analogues of Inorganic Layered Materials. *Angew. Chem., Int. Ed.* **2013**, *52*, 13162−13185.

(4) Wang, Q. H.; Kalantar-Zadeh, K.; Kis, A.; Coleman, J. N.; Strano, M. S. Electronics and Optoelectronics of Two-Dimensional Transition Metal Dichalcogenides. *Nat. Nanotechnol.* **2012**, *7*, 699−712.

(5) van der Stam, W.; Akkerman, Q. A.; Ke, X.; van Huis, M. A.; Bals, S.; de Mello Donega, C. Solution-Processable Ultrathin Size- and Shape-Controlled Colloidal $Cu_{2-x}S$ Nanosheets. *Chem. Mater.* **2015**, *27*, 283−291.

(6) Nasilowski, M.; Mahler, B.; Lhuillier, E.; Ithurria, S.; Dubertret, B. Two-Dimensional Colloidal Nanocrystals. *Chem. Rev.* **2016**, *116*, 10934−10982.

(7) Novoselov, K. S.; Fal, V. I.; Colombo, L.; Gellert, P. R.; Schwab, M. G.; Kim, K.; Fal'ko, V. I.; Colombo, L.; Gellert, P. R.; Schwab, M. G.; et al. A Roadmap for Graphene. *Nature* **2013**, *490*, 192−200.

(8) Du, Y.; Yin, Z.; Zhu, J.; Huang, X.; Wu, X.-J.; Zeng, Z.; Yan, Q.; Zhang, H. A General Method for the Large-Scale Synthesis of Uniform Ultrathin Metal Sulphide Nanocrystals. *Nat. Commun.* **2012**, *3*, 1177.

(9) Berends, A. C.; de Mello Donegá, C. Ultrathin One- and Two-Dimensional Colloidal Semiconductor Nanocrystals: Pushing Quantum Confinement to the Limit. *J. Phys. Chem. Lett.* **2017**, *8*, 4077−4090.

(10) Wang, F.; Wang, Y.; Liu, Y.-H.; Morrison, P. J.; Loomis, R. A.; Buhro, W. E. Two-Dimensional Semiconductor Nanocrystals: Properties, Templated Formation, and Magic-Size Nanocluster Intermediates. *Acc. Chem. Res.* **2015**, *48*, 13−21.

(11) Zhang, H. Ultrathin Two-Dimensional Nanomaterials. *ACS Nano* **2015**, *9*, 9451−9469.

(12) Zhang, Y.; Lu, J.; Shen, S.; Xu, H.; Wang, Q. Ultralarge Single Crystal SnS Rectangular Nanosheets. *Chem. Commun.* **2011**, *47*, 5226−5228.

(13) Li, L.; Chen, Z.; Hu, Y.; Wang, X.; Zhang, T.; Chen, W.; Wang, Q. Single-Layer Single-Crystalline SnSe Nanosheets. *J. Am. Chem. Soc.* **2013**, *135*, 1213−1216.

(14) Lauth, J.; Gorris, F. E. S.; Samadi Khoshkhoo, M.; Chassé, T.; Friedrich, W.; Lebedeva, V.; Meyer, A.; Klinke, C.; Kornowski, A.; Scheele, M.; et al. Solution-Processed Two-Dimensional Ultrathin InSe Nanosheets. *Chem. Mater.* **2016**, *28*, 1728−1736.

(15) Almeida, G.; Dogan, S.; Bertoni, G.; Giannini, C.; Gaspari, R.; Perissinotto, S.; Krahne, R.; Ghosh, S.; Manna, L. Colloidal Monolayer β-In_2Se_3 Nanosheets with High Photoresponsivity. *J. Am. Chem. Soc.* **2017**, *139*, 3005−3011.

(16) Deng, Z.; Mansuripur, M.; Muscat, A. J. Synthesis of Two-Dimensional Single-Crystal Berzelianite Nanosheets and Nanoplates with near-Infrared Optical Absorption. *J. Mater. Chem.* **2009**, *19*, 6201−6206.

(17) Mahler, B.; Hoepfner, V.; Liao, K.; Ozin, G. A. Colloidal Synthesis of 1T-WS_2 and 2H-WS_2 Nanosheets: Applications for Photocatalytic Hydrogen Evolution. *J. Am. Chem. Soc.* **2014**, *136*, 14121−14127.

(18) Jung, W.; Lee, S.; Yoo, D.; Jeong, S.; Miró, P.; Kuc, A.; Heine, T.; Cheon, J. Colloidal Synthesis of Single-Layer MSe_2 (M = Mo, W) Nanosheets via Anisotropic Solution-Phase Growth Approach. *J. Am. Chem. Soc.* **2015**, *137*, 7266−7269.

(19) Binsma, J. J. M.; Giling, L. J.; Bloem, J. Luminescence of $CuInS_2$. II Exciton and near Edge Emission. *J. Lumin.* **1982**, *27*, 55−72.

(20) Ueng, H. Y.; Hwang, H. The Defect Structure of $CuInS_2$. Part I: Intrinsic Defects. *J. Phys. Chem. Solids* **1989**, *50*, 1297−1305.

(21) Jaffe, J.; Zunger, A. Electronic Structure of the Ternary Chalcopyrite Semiconductors $CuAlS_2$, $CuGaS_2$, $CuInS_2$, $CuAlSe_2$, $CuGaSe_2$, and $CuInSe_2$. *Phys. Rev. B: Condens. Matter Mater. Phys.* **1983**, *28*, 5822−5847.

(22) Kolny-Olesiak, J.; Weller, H. Synthesis and Application of Colloidal $CuInS_2$ Semiconductor Nanocrystals. *ACS Appl. Mater. Interfaces* **2013**, *5*, 12221−12237.

DOI: 10.1021/acs.chemmater.7b04925
Chem. Mater. 2017, 29, 10551−10560

(23) Berends, A. C.; Rabouw, F. T.; Spoor, F. C. M.; Bladt, E.; Grozema, F. C.; Houtepen, A. J.; Siebbeles, L. D. A.; de Mello Donegá, C. Radiative and Nonradiative Recombination in $CuInS_2$ Nanocrystals and $CuInS_2$ -Based Core/Shell Nanocrystals. *J. Phys. Chem. Lett.* **2016**, *7*, 3503−3509.
(24) van der Stam, W.; Berends, A. C.; de Mello Donegá, C. Prospects of Colloidal Copper Chalcogenide Nanocrystals. *ChemPhysChem* **2016**, *17*, 559−581.
(25) Xia, C.; Meeldijk, J. D.; Gerritsen, H. C.; de Mello Donega, C. Highly Luminescent Water-Dispersible NIR-Emitting Wurtzite $CuInS_2$/ZnS Core/Shell Colloidal Quantum Dots. *Chem. Mater.* **2017**, *29*, 4940−4951.
(26) van der Stam, W.; Berends, A. C.; Rabouw, F. T.; Willhammar, T.; Ke, X.; Meeldijk, J. D.; Bals, S.; de Mello Donega, C. Luminescent $CuInS_2$ Quantum Dots by Partial Cation Exchange in $Cu_{2-x}S$ Nanocrystals. *Chem. Mater.* **2015**, *27*, 621−628.
(27) van der Stam, W.; Bladt, E.; Rabouw, F. T.; Bals, S.; de Mello Donega, C. Near-Infrared Emitting $CuInSe_2$/$CuInS_2$ Dot Core/Rod Shell Heteronanorods by Sequential Cation Exchange. *ACS Nano* **2015**, *9*, 11430−11438.
(28) Mu, L.; Wang, F.; Buhro, W. E. Exciton Splitting in Thin Copper Indium Disulfide Nanosheets. *Chem. Mater.* **2017**, *29*, 3686−3693.
(29) Bryks, W.; Lupi, E.; Ngo, C.; Tao, A. R. Digenite Nanosheets Synthesized by Thermolysis of Layered Copper-Alkanethiolate Frameworks. *J. Am. Chem. Soc.* **2016**, *138*, 13717−13725.
(30) Hessel, C. M.; Pattani, V. P.; Rasch, M.; Panthani, M. G.; Koo, B.; Tunnell, J. W.; Korgel, B. A. Copper Selenide Nanocrystals for Photothermal Therapy. *Nano Lett.* **2011**, *11*, 2560−2566.
(31) Liu, X.; Law, W.-C.; Jeon, M.; Wang, X.; Liu, M.; Kim, C.; Prasad, P. N.; Swihart, M. T. $Cu_{2-x}Se$ Nanocrystals with Localized Surface Plasmon Resonance as Sensitive Contrast Agents for In Vivo Photoacoustic Imaging: Demonstration of Sentinel Lymph Node Mapping. *Adv. Healthcare Mater.* **2013**, *2*, 952−957.
(32) Runnerstrom, E. L.; Llordés, A.; Lounis, S. D.; Milliron, D. J. Nanostructured Electrochromic Smart Windows: Traditional Materials and NIR-Sensitive Plasmonic Nanomaterials. *Chem. Commun.* **2014**, *50*, 10555−10572.
(33) Bekenstein, Y.; Vinokurov, K.; Keren-Zur, S.; Hadar, I.; Schilt, Y.; Raviv, U.; Millo, O.; Banin, U. Thermal Doping by Vacancy Formation in Copper Sulfide Nanocrystal Arrays. *Nano Lett.* **2014**, *14*, 1349−1353.
(34) Li, L.; Pandey, A.; Werder, D. J.; Khanal, B. P.; Pietryga, M.; Klimov, V. I. Efficient Synthesis of Highly Luminescent Copper Indium Sulfide-Based Core/Shell Nanocrystals with Surprisingly Long-Lived Emission. *J. Am. Chem. Soc.* **2011**, *133*, 1176−1179.
(35) Klinger, M.; Jäger, A. Crystallographic Tool Box (CrystTBox): Automated Tools for Transmission Electron Microscopists and Crystallographers. *J. Appl. Crystallogr.* **2015**, *48*, 2012−2018.
(36) Kresse, G.; Joubert, D. From Ultrasoft Pseudopotentials to the Projector Augmented-Wave Method. *Phys. Rev. B: Condens. Matter Mater. Phys.* **1999**, *59*, 1758−1775.
(37) Perdew, J. P.; Burke, K.; Ernzerhof, M. Generalized Gradient Approximation Made Simple. *Phys. Rev. Lett.* **1996**, *77*, 3865−3868.
(38) Kresse, G.; Hafner, J. Ab Initio Molecular Dynamics for Liquid Metals. *Phys. Rev. B: Condens. Matter Mater. Phys.* **1993**, *47*, 558−561.
(39) Kresse, G.; Furthmüller, J. Efficiency of Ab-Initio Total Energy Calculations for Metals and Semiconductors Using a Plane-Wave Basis Set. *Comput. Mater. Sci.* **1996**, *6*, 15−50.
(40) Kushwaha, P.; Patra, A.; Anjali, E.; Surdi, H.; Singh, A.; Gurada, C.; Ramakrishnan, S.; Prabhu, S. S.; Gopal, A. V.; Thamizhavel, A. Physical, Optical and Nonlinear Properties of InS Single Crystal. *Opt. Mater.* **2014**, *36*, 616−620.
(41) Klimeš, J.; Bowler, D. R.; Michaelides, A. Chemical Accuracy for the van der Waals Density Functional. *J. Phys.: Condens. Matter* **2010**, *22*, 022201.
(42) Thomson, J. W.; Nagashima, K.; Macdonald, P. M.; Ozin, G. A. From Sulfur-Amine Solutions to Metal Sulfide Nanocrystals: Peering into the Oleylamine- Sulfur Black Box. *J. Am. Chem. Soc.* **2011**, *133*, 5036−5040.
(43) Xie, Y.; Riedinger, A.; Prato, M.; Casu, A.; Genovese, A.; Guardia, P.; Sottini, S.; Sangregorio, C.; Miszta, K.; Ghosh, S.; et al. Copper Sulfide Nanocrystals with Tunable Composition by Reduction of Covellite Nanocrystals with Cu^+ Ions. *J. Am. Chem. Soc.* **2013**, *135*, 17630−17637.
(44) Wang, L.-W. High chalcocite Cu_2S: a solid-liquid hybrid phase. *Phys. Rev. Lett.* **2012**, *108*, 085703.
(45) van der Stam, W.; Rabouw, F. T.; Geuchies, J. J.; Berends, A. C.; Hinterding, S. O. M.; Geitenbeek, R. G.; van der Lit, J.; Prévost, S.; Petukhov, A. V.; de Mello Donega, C. *In Situ* Probing of Stack-Templated Growth of Ultrathin $Cu_{2-x}S$ Nanosheets. *Chem. Mater.* **2016**, *28*, 6381−6389.
(46) Morrison, P. J.; Loomis, R. A.; Buhro, W. E. Synthesis and Growth Mechanism of Lead Sulfide Quantum Platelets in Lamellar Mesophase Templates. *Chem. Mater.* **2014**, *26*, 5012−5019.
(47) Ithurria, S.; Bousquet, G.; Dubertret, B. Continuous Transition from 3D to 1D Confinement Observed During the Formation of CdSe Nanoplatelets. *J. Am. Chem. Soc.* **2011**, *133*, 3070−3077.
(48) Riedinger, A.; Ott, F. D.; Mule, A.; Mazzotti, S.; Knüsel, P. N.; Kress, S. J. P.; Prins, F.; Erwin, S. C.; Norris, D. J. An Intrinsic Growth Instability in Isotropic Materials Leads to Quasi-Two-Dimensional Nanoplatelets *Nat. Mater.* **2017**, DOI: 10.1038/nmat4889.
(49) Tang, Z.; Zhang, Z.; Wang, Y.; Glotzer, S. C.; Kotov, N. A. Self-Assembly of CdTe Nanocrystals into Free-Floating Sheets. *Science* **2006**, *314*, 274−278.
(50) Srivastava, S.; Santos, A.; Critchley, K.; Kim, K.; Podiadlo, P.; Sun, K.; Lee, J.; Xu, C.; Lilly, G.; Gotzer, S.; et al. Light-Controlled Self-Assemby of Semiconductor Nanoparticles into Twisted Ribbons. *Science* **2010**, *327*, 1355−1359.
(51) Yeom, J.; Yeom, B.; Chan, H.; Smith, K. W.; Dominguez-Medina, S.; Bahng, J. H.; Zhao, G.; Chang, W.-S.; Chang, S.-J.; Chuvilin, A.; et al. Chiral Templating of Self-Assembling Nanostructures by Circularly Polarized Light. *Nat. Mater.* **2015**, *14*, 66−72.
(52) Donega, C. d. M. Synthesis and Properties of Colloidal Heteronanocrystals. *Chem. Soc. Rev.* **2011**, *40*, 1512−1546.

DOI: 10.1021/acs.chemmater.7b04925
Chem. Mater. 2017, 29, 10551−10560